Structuring Electrodes via Acoustic-Field-Assisted Particle Patterning for Enhanced Performance of Lithium-Ion Batteries

Yifan Zhang, M Shahriar, Shan Hu*

Department of Mechanical Engineering, Iowa State University, Ames, Iowa 50011, USA

* Corresponding author: shanhu@iastate.edu

Abstract

The sluggish mass transport in current battery electrodes limits their performance, especially at high-rate cycling, and even negatively impacts the energy density. In this study, we report an acoustic-field-assisted particle patterning method to generate ordered structures in $LiFePO_4$ (LFP) and $Li_4Ti_5O_{12}$ (LTO) electrodes to facilitate lithium-ion diffusion and charge transport kinetics in these electrodes. With areal mass loading up to 18 mg/cm^2, LFP and LTO electrodes produced by our acoustic field-based method deliver 165.8 and 173.5 mAh/g at 0.1 C, respectively, and maintain up to 51% of theoretical capacity at rate up to 5 C, showing superior rate capability over the ones fabricated via conventional casting. This work represents a novel and effective strategy to engineer the electrode structure for enhancing the performance of electrodes in LIBs.

Keywords: Lithium-ion batteries, acoustic-assisted particle patterning, electrode structural engineering, ion diffusion, charge transport kinetics, rate capability, cycling stability

1. Introduction

Lithium-ion battery (LIB) is a key enabler for decarbonizing the energy and transportation sectors[1,2]. To compete with traditional fossil energy, LIB's performance needs to be further improved and its cost needs to be further reduced[3]. Currently, LIB electrodes display significant loss of capacity at relatively high charge/discharge rates. Such a performance loss is especially severe for electrodes with high tortuosity [4–7]. Tortuosity measures the average length that an ion travels from the bulk electrolyte to the reaction site at the electrode-electrolyte interface. Based on the relation between tortuosity and ionic diffusivity in a porous electrode, which is defined as $D_{eff} = \varepsilon D_0/\tau$, where τ and ε represent tortuosity and fraction of pores (assumed filled with electrolyte) in the electrode, respectively; D_0 and D_{eff} represent intrinsic and effective ionic diffusivity, respectively[8]. Higher tortuosity in the electrode induces slower diffusion of lithium ions. At high charge/discharge rate, the slow ion transport means there is only enough time for the ions to reach electrode materials closest to the bulk electrolyte, consequently only a small fraction of the electrode contributes to the energy storage reaction, which greatly limits the capacity and energy/power density[9–12]. Furthermore, the uneven utilization of electrode materials causes non-uniform mechanical stress and phase transition in the electrode, leading to cracking/delamination that accelerates the aging of the electrode. Existing work showed that an effective way to reduce tortuosity is to introduce ordered structures such as aligned slit channels, through-thickness holes, etc. As a result, currently there are concerted efforts on engineering the electrode structure, through methods such as laser drilling[13], magnetic field alignment[14–18], ice templating[19–27]. However, these

methods either require adding "foreign" materials (e.g., magnetic fluids for magnetic field alignment and ice for ice-templating) or "subtractive" manufacturing which removes part of the electrode materials (e.g., laser drilling).

Herein, inspired by works that used acoustic field to manipulate particles in microfluidic devices[28–36], we developed an acoustic-field-assisted particle patterning (AP) method to construct highly ordered structures in battery electrodes. In a typical AP-based electrode manufacturing process, electrode slurry containing electrode particles (i.e., active material and conductive additive particles) and binder solution is initially coated onto the current collector. Then a standing acoustic wave will be established in the slurry, which exerts acoustic radiation force to move the electrode particles to the acoustic nodes and away from the acoustic antinodes, thus forming voids near the acoustic antinodes after the binder solvent is evaporated. The standing acoustic wave patterns largely determine the morphology of the voids. This method possesses several advantages over the existing methods for fabricating 3D-structured battery electrodes. Firstly, acoustic-field-assisted particle patterning does not require particles to be susceptible to electrical, magnetic, optical, or thermal stimulus, rather it only requires there is density difference between the electrode particles and their surrounding media (e.g., the binder solution). Hence, the AP method can be applied to pattern a wide range of electrode particles as demonstrated in this study with $LiFePO_4$ (LFP) and $Li_4Ti_5O_{12}$ (LTO) particles. Second, the AP method directly works on the "native" active material particles to control their spatial distribution and does not need any "foreign" additives that are responsive to external stimulation or any sacrificing templates for constructing 3D structures, thus waving the need for post-processing to remove these additives and templates. Moreover, the AP method is nondestructive and will not induce chemical or physical damage to the electrode materials. Last but not least, during the AP-based electrode fabrication process no solid-state particles in the electrode need to be removed which reduces materials waste.

Using the AP method, we fabricated 3D-structured battery electrodes with aligned channels and aligned through-holes, which serves as low-tortuosity ion diffusion pathways. The acoustically processed electrodes outperform the ones fabricated with conventional casting (CC) method with equal areal mass loading. Specifically, LFP and LTO electrodes fabricated by AP method maintain specific capacity of 32% and 51% at a rate of 5 C, respectively, while electrodes from CC method struggle to deliver at the same rate. In many prior studies, retaining the specific capacity at high rate has often come at the cost of a low volumetric energy density. However, the volumetric energy densities of the acoustically processed electrodes are consistently higher at all cycling rates than that of CC electrode of the same chemistry at the same areal mass loading. Furthermore, the long-term charge and discharge cycling test demonstrates the improvement of cycling stability of acoustically patterned electrodes. These results demonstrate that acoustic-assisted particle patterning can be an effective method to engineer electrode structures for enhanced energy, power, and cycling stability performances.

2. Materials and Methods

2.1 Generation of Standing Acoustic Wave

Standing acoustic wave (SAW) will be generated to manipulate the solid components in the slurry. The experimental setup of SAW generation consists of an arbitrary function generator (DG1022, Rigol Technologies, Inc.), a signal amplifier (2350 Precision Power Amplifier, TEGAM Inc.) and

four piezoelectric transducer (PZT) plates (20x15x1.4 mm 1.5 MHz, Steiner & Martins, Inc.). The vibration frequency and amplitude of target acoustic wave are tuned through function generator. The PZTs were coupled to the aluminum foil of dimension of 80x60 mm using vacuum grease. As shown in Fig. 1, during the experiment, a 3D-printed supporting tray holds the PZTs in a rectangular housing and four pieces of PZTs were placed on each side of the current collector at a 90-degree angle. When a sinusoidal voltage of certain frequency and amplitude was applied to one PZT, the activated PZT will generate acoustic wave (the incident wave) propagating along the surface of the current collector. The inactivated PZT directly facing the activated one will work as uniform solid boundary layer to reflect the incident wave. The reflected and incident waves will form a SAW between the two PZTs facing each other. SAW will then transmit into the electrode slurry on top of the current collector to manipulate the solid components.

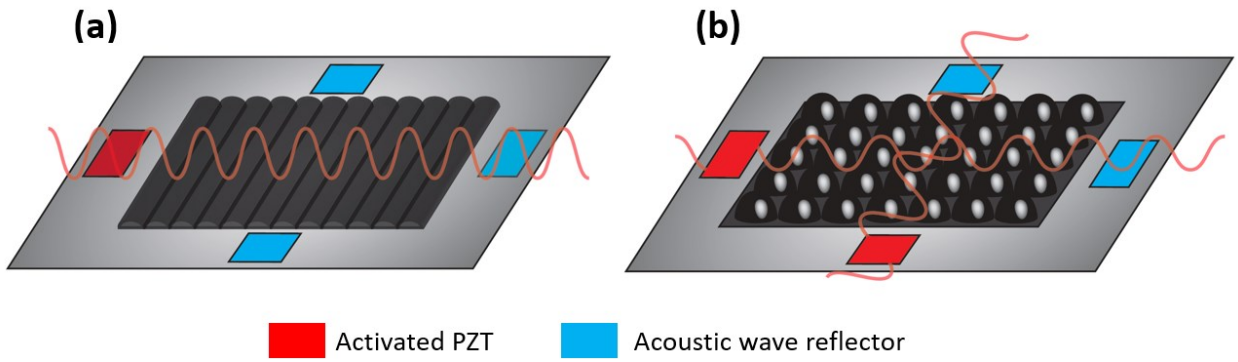

Fig. 1 Schematic working mechanism of acoustic-field-assisted electrode patterning.

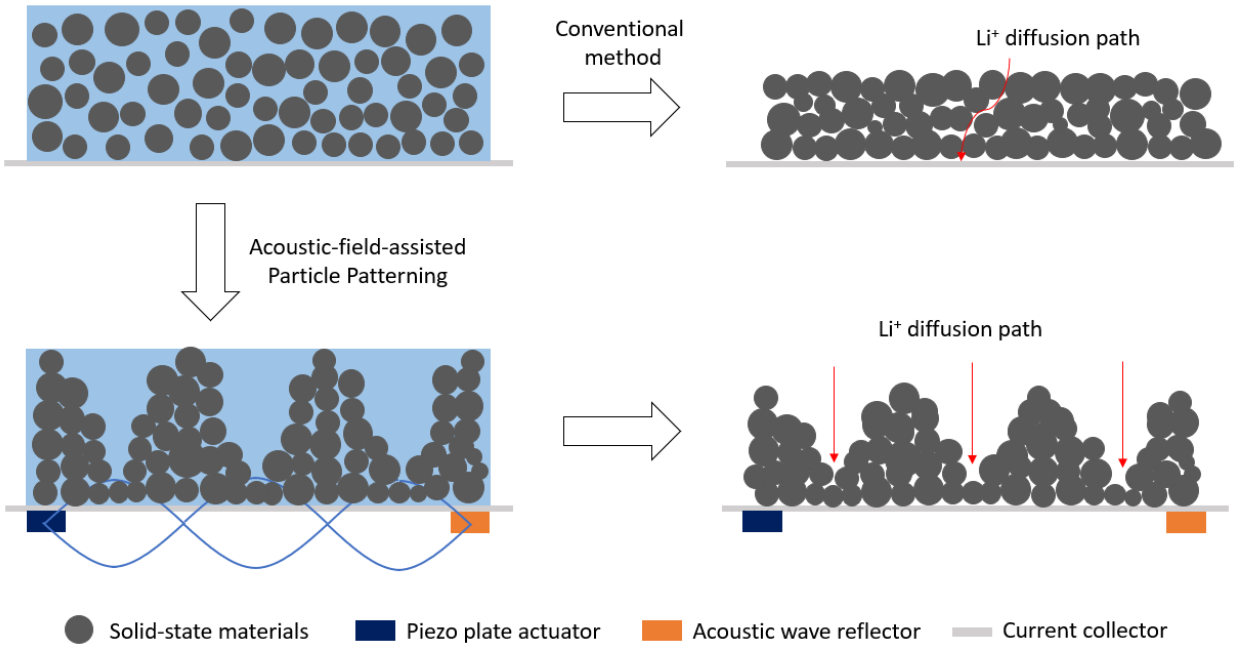

Fig. 2 Schematic illustration of electrode fabrication via acoustic-field-assisted patterning (AP) method and conventional casting (CC) method.

The key to construct 3D structures in the battery electrodes with the AP method is to align solid components in the colloidal system by the primary acoustic radiation force from the SAW, which is defined as:

$$F_{pr} = -\left(\frac{\pi p_0^2 V_p \beta_f}{2\lambda}\right) \varphi(\beta, \rho) \sin(2kx) \quad (1)$$

where p_0 and V_p represent acoustic pressure and volume of particle, respectively; β and ρ represent compressibility and density, respectively; k and λ represent wavevector and wavelength, respectively. In the equation (1), φ stands for the contrast factor as a function of compressibility and density, which is expressed as:

$$\varphi(\beta, \rho) = \frac{5\rho_p - 2\rho_f}{2\rho_p + \rho_f} - \frac{\beta_p}{\beta_f} \quad (2)$$

where subscript p and f stand for particle and fluid, respectively. In this study, the solid contents in the electrode slurry consist of LFP or LTO particles as the active materials and acetylene black as conductive additives. The solid contents that have larger densities are dispersed within a binder solution (fluid phase) that has a lower density. In addition, the compressibility of the solid particles is far less than the fluid ($\beta_p \ll \beta_f$), leading the second term in equation (2) close to zero. Typically, given that the contrast factor is greater than zero, solid particles will move towards the nodes of sinusoidal wave as Fig. 2 illustrates. Once the movement of particles commences, Stokes drag force also applies to the particles, which is expressed as:

$$F_d = 6\pi\mu r v_p \quad (3)$$

where μ represents the dynamic viscosity of liquid medium; r and v_p represent radius and the velocity of the particle, respectively. Therefore, if the primary acoustic radiation force is large enough for solid components to overcome the resistance from Stokes drag force in liquid medium, the alignment of active material particles is achievable.

2.2 Fabrication of Electrode

The electrode slurry was prepared by mixing active materials (LFP powder: D50 = 1.5 μm and LTO powder: D50 = 5.0 ~ 10.0 μm, MSE Supplies), poly(vinyl alcohol) (PVA) binder (Mowiol 40-88, M_w ~ 205,000 g/mol, Sigma-Aldrich) and acetylene black (Alfa Aesar, 100% compressed) with mass ratio of 85:5:10 in deionized water followed by mechanical stirring overnight to achieve a homogeneous mixture. The slurry was then cast on aluminum foil (15 μm thick, MTI Corporation) with the doctor blade. The cast film and the aluminum substrate were then coupled to the acoustic-field-assisted particle patterning platform using vacuum grease (Dow Corning). To pattern the electrode particles (both active materials and acetylene black), sinusoidal signal of 80 kHz frequency and 160 V peak-to-peak amplitude was applied to one PZT plate to generate line patterns and to two adjacent PZT plates to generate grid patterns. After the particle pattern stabilized, the

wet electrode was initially dried for two hours at room temperature with the acoustic field on. Afterwards, the dried electrode was transferred into a vacuum oven for further drying at 100 ℃ overnight before it was cut and assembled into a coin cell for testing. For comparison, conventional casting LFP and LTO electrodes were prepared with the same procedure without the AP process.

2.3 Structural and Electrochemical Characterization

The morphology of the top surface of electrode was examined by confocal microscopy (VK-X3000 series 3D surface profiler, Keyence), and the cross-sections of electrode were characterized by scanning electron microscopy and energy dispersive spectroscopy (EDS) (FEI Inspect F50 SEM). X-ray diffraction (XRD) studies of the acoustically processed electrodes were conducted with Rigaku Smartlab x-ray diffractometer (Cu Kα radiation).

For electrochemical tests, half cells were assembled as CR2032 coin cells inside a glovebox (O_2 and moisture < 0.5 ppm) with LFP or LTO electrode as the working electrode, a lithium disk as counter electrode, and one layer of porous polymer separator (Celgard 2400) in-between soaked in electrolyte of 1 M $LiPF_6$ dissolved in 3:7 mass ratio of ethylene carbonate (EC) and ethyl methyl carbonate (EMC). Cyclic voltammetry (CV) was measured at scan rates ranging from 0.1 to 0.25 mV/s and electrochemical impedance spectroscopy (EIS) was tested with frequency from 1 MHz to 0.1 Hz with AC voltage of 10 mV on an electrochemical working station (Gamry Reference 3000). For the galvanostatic test, the cell was charged at various C-rates (1 C = 170 mA/g for LFP and 175 mA/g for LTO) to 4.2 V for LFP or 2.5 V for LTO and held at the same voltage until current drops to 0.05 C, followed by discharging at the corresponding C-rates until voltage drops to 2.2 V for LFP or 1.0 V for LTO during the same cycle, using a battery test system (LANDT CT3001A). Full cells were assembled by LFP and LTO as cathode and anode, respectively, with N/P ratio controlled as 1.2. For both rate capability and long-term cycling tests of full cells, all the sample cells were cycled between 1.0 V and 2.4 V at various C-rates. Before the galvanostatic test and the long-term cycling test, all the full cells were charged and discharged at 0.1 C for 2 cycles as formation cycles.

3. Results and Discussion

3.1 3D Structures of Electrodes Processed by Acoustic-Field-Assisted Particle Patterning

The confocal microscopy images in Fig. 3 illustrate the top surface morphology of the LFP and LTO electrodes fabricated with the AP method and that of the ones with conventional casting (CC) method. Regions with color red in the images represent the “peaks” of the surface profile while those with dark blue colors represent the “valleys” or “holes”. Fig. 3 (a-b) and (c-d) clearly show that two types of surface morphology patterns were generated for LFP and LTO electrodes by the AP method: “grids” and “aligned lines”. When only one PZT is activated, aligned lines are observed in the electrodes denoted as L-LFP and L-LTO. When two adjacent PZTs are activated, grid patterns are observed, which are denoted as G-LFP, G-LTO. Whereas the confocal images of electrodes fabricated by CC method (denoted as CC-LFP and CC-LTO) do not show any patterns (Fig. S1). By comparing the surface morphologies to the simulated acoustic pressure patterns shown in Fig. S3, it can be seen that the solid component particles are concentrated near the nodes (low pressure region) of the acoustic field, and they form the “peaks” in these regions as observed

in the confocal images. On the other hand, particles are removed from the acoustic antinodes creating “valleys” in these areas.

The cross-sectional area of LFP and LTO electrodes processed by the AP method is illustrated by the SEM images shown in Fig. 4. The inverted-cone-shaped holes were generated on the electrodes (Fig. 4a and 4b) when two adjacent PZTs are activated as confirmed by the cross-sectional SEM images and the top morphology confocal images (Fig. 3a and 3b). The distance between adjacent peak and hole is found to be around 400 μm from both the confocal and SEM images. On the other hand, the alternating peak-and-valley structures of the cross-sectional areas observed from the SEM images (Fig. 4c and 4d) and the top surface morphology observed from the confocal images (Fig. 3c and 3d) confirm that aligned lines were generated in the L-LFP and L-LTO electrodes by the AP method when only one PZT is activated. The distance between adjacent peak and valley is found to be around 400 μm from both the confocal and SEM images. Even distribution of the elements can be observed from the EDS elemental mappings of the top surfaces and the cross-sectional areas of the acoustically patterned electrodes (Fig. S4-S11). This demonstrates that although the acoustic field concentrates the solid components to the acoustic nodes, it causes no stratification of active materials and carbon additives in the patterned electrodes, which guarantees electrical conduction to all areas of the electrode. As shown in Fig. 4e and 4f, the XRD diffraction patterns of the acoustically processed electrodes (i.e., G-LFP and L-LFP, G-LTO and L-LTO) match the those of the pristine LFP and LTO powder, respectively, confirming that the AP method does not change the crystal structure of the active materials.

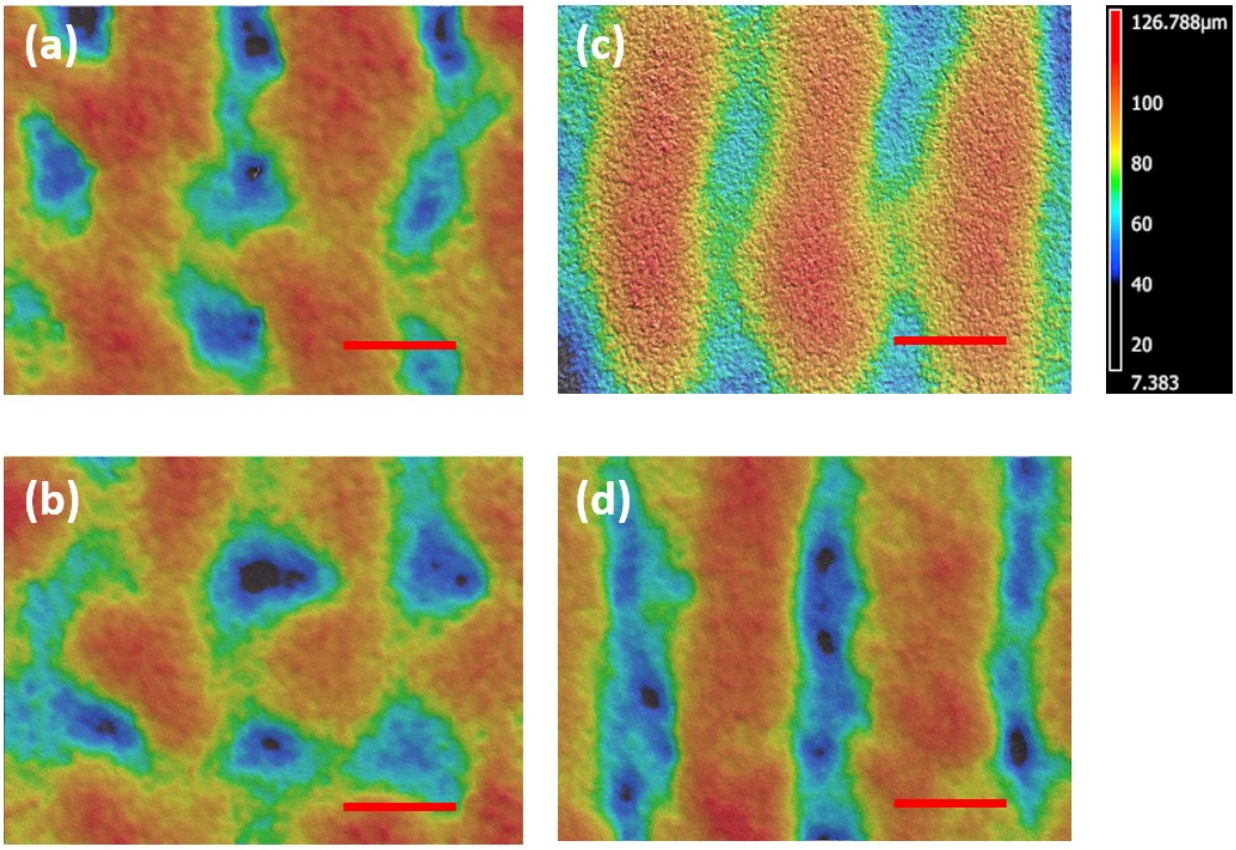

Fig. 3 Confocal microscopy images of (a) G-LFP, (b) G-LTO, (c) L-LFP, (d) L-LTO (scale bar: 500-μm).

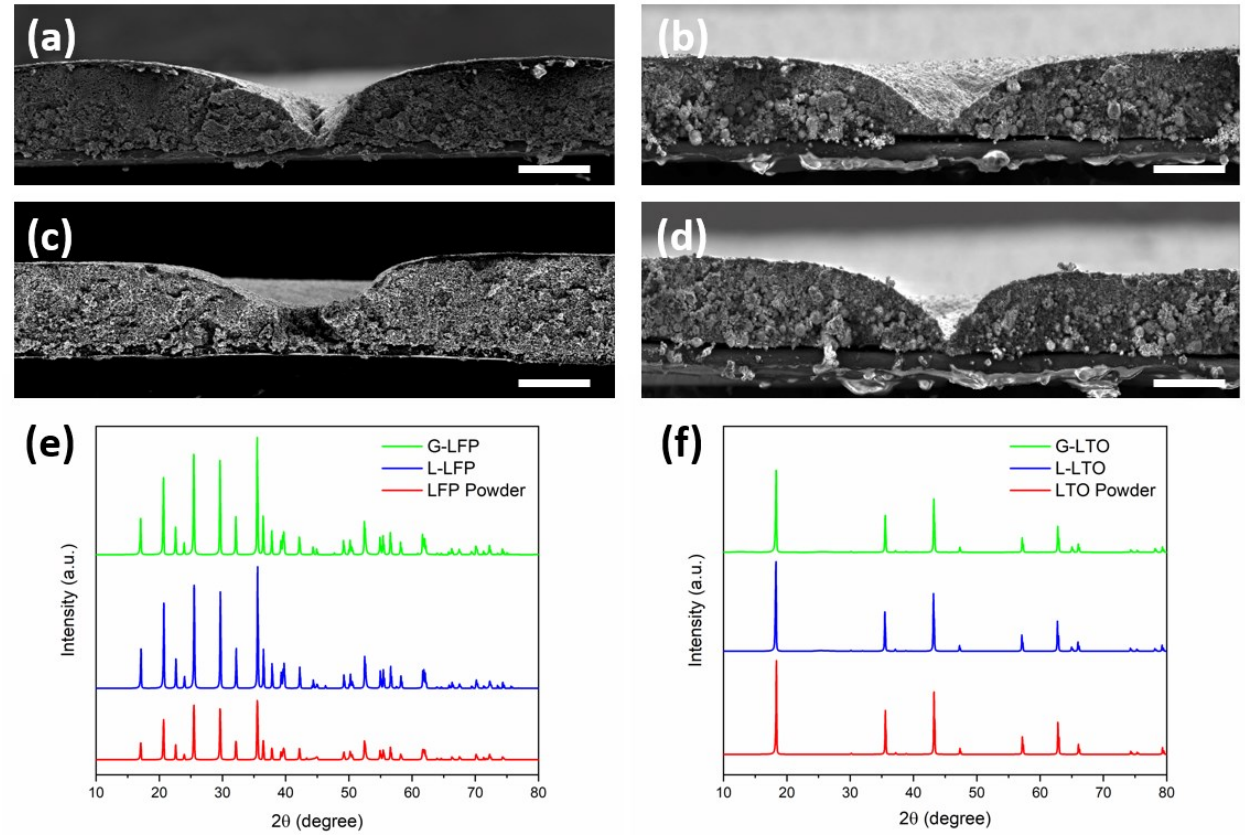

Fig. 4 Electrode Characterizations: SEM images of cross-sectional area of (a) G-LFP, (b) G-LTO, (c) L-LFP, (d) L-LTO (scale bar: 100-μm). XRD patterns of (e) acoustically processed LFP electrodes and pristine LFP powder and (f) acoustically processed LTO electrodes and pristine LTO powder.

3.2 Electrochemical performance

To investigate the advantages of 3D-structured electrodes patterned by the AP method in terms of diffusion of lithium ions, cyclic voltammetry (CV) analysis is performed. For the measurement of CV, a series of scan rates from 0.1 to 0.25 mV/s were applied to both LFP and LTO electrodes. Compared to the CC-LFP and CC-LTO electrode, higher peak current and narrower redox peaks at the same scan rate are observed in the CV of electrodes produced via AP method. Example cyclic voltammograms of both LFP and LTO half-cells scanned at 0.1 mV/s are compared with CV of CC half-cells at the same rate in Fig. S12c and S12d. In a diffusion-controlled redox reaction, according to Randles-Sevcik equation, peak current (i_p) is linearly related to the square root of scan rate ($\nu^{1/2}$). With the same electrode area in the testing cell, the slope of the i_p versus $\nu^{1/2}$ line, is affected by the diffusion coefficient of lithium ions (D_{Li^+}). After linear fitting, the slope of the i_p versus $\nu^{1/2}$ lines can be obtained to calculate the diffusion coefficient as discussed in Electronic

Supplementary Information. The slopes and the calculated D_{Li+} are listed in Table S1. G-LFP electrode, for instance, shows higher D_{Li+} of 4.73×10^{-9} and 2.75×10^{-9} cm^2/s in charge and discharge process, respectively (Fig. 5f), than CC-LFP electrode (2.22×10^{-9} cm^2/s in charge process and 5.95×10^{-10} cm^2/s and in discharge process). Similarly, the aligned structure in LFP and LTO electrodes also demonstrate an enhanced diffusivity of lithium ions, and detailed values are listed in Table S1. The result of CV analysis reveals that the aligned valleys and through-holes in the electrode generated through our manufacturing method facilitate lithium-ion diffusion, which is essential to maintain the high areal capacity especially at high rates.

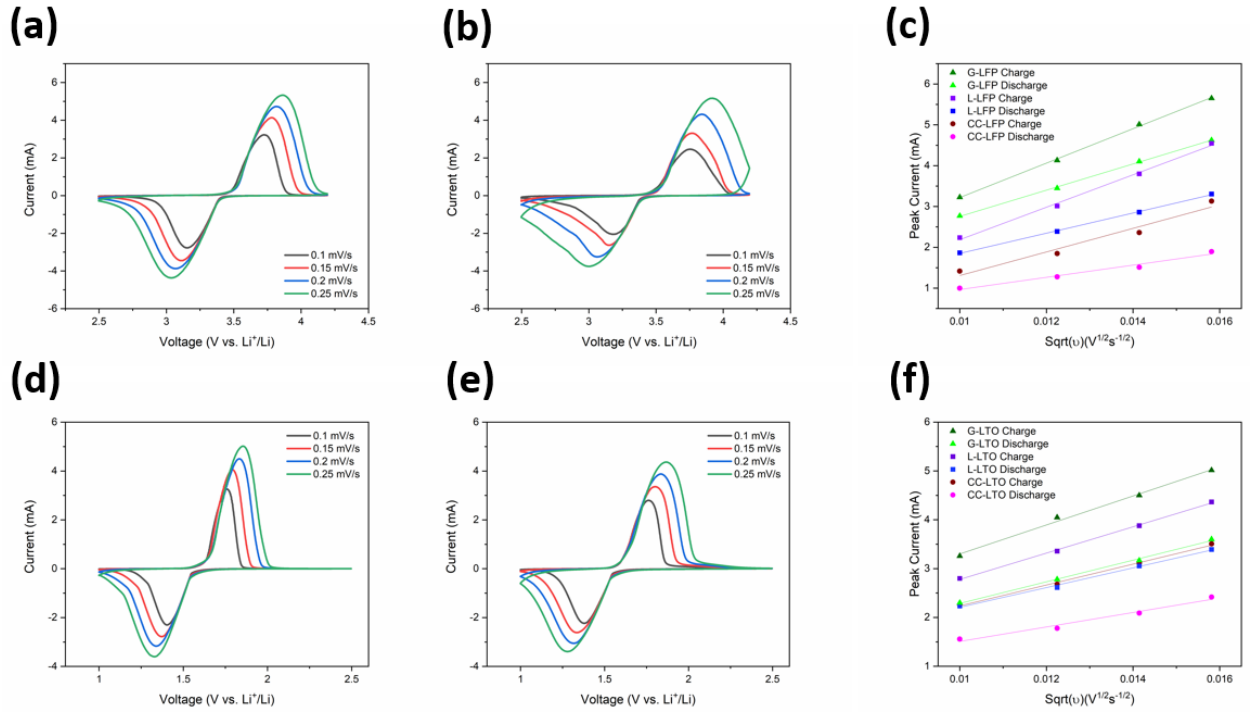

Fig. 5 Cyclic voltammograms of (a) G-LFP, (b) L-LFP, (d) G-LTO and (e) L-LTO at scan rate of 0.1, 0.15, 0.2 and 0.25 mV/s; Comparison of linear fitting of peak current against square root of scan rate among two patterned electrodes and conventionally fabricated electrodes based on (c) LFP and (f) LTO.

Additionally, galvanostatic intermittent titration technique (GITT) was also implemented to characterize the lithium-ion diffusion coefficient of the electrodes. From Fig. 6 (a-d) and Fig. S13, although similar static potentials are observed in all samples with respect to the active material (3.43 V for LFP electrodes and 1.56 V for LTO electrodes), the conventionally fabricated electrodes demonstrate larger overpotential than the acoustically patterned ones. Based on the GITT profiles, the lithium-ion diffusion coefficients of G-LFP and L-LFP electrodes are calculated as 3.31×10^{-9} cm^2/s and 2.79×10^{-9} cm^2/s, respectively, both higher than that of CC-LFP electrode (1.51×10^{-9} cm^2/s). Detailed explanation on how the lithium-ion diffusion coefficients (D_{Li+}) are calculated from GITT results is given in Electronic Supplementary Information and the calculated D_{Li+} values are listed in Table S2. Meanwhile, compared to CC-LTO electrode, G-LTO and L-LTO electrode also show advantageous diffusion behavior (Table S2). This enhancement of lithium-ion diffusion is attributed to the structures constructed in the electrodes. The lithium-ion

diffusion coefficients derived from GITT studies are consistent with the results of CV investigation for all electrodes.

The electrochemical impedance spectroscopy (EIS) Nyquist plots of two types of active materials fabricated by the AP and CC method are shown in Fig. 6e and 6f, respectively. The internal resistance (R_u) is located at the intercept of curve on Re(Z) axis in the high-frequency region, followed by a quasi-semi-circle in the middle-frequency region, and charge transfer resistance (R_{ct}) is estimated by the second intercept on Re(Z) axis by the quasi-semi-circle of each Nyquist plot. An equivalent circuit shown in Fig. S15a was used to fit the EIS data to obtain the values of R_u and R_{ct}. As shown in the Nyquist plots (Fig. 6e and 6f, Table S3), both acoustically patterned LFP and LTO electrodes have lower charge transfer resistance (G-LFP: 50.7 Ω, L-LFP: 90.6 Ω; G-LTO: 226.3 Ω, L-LTO: 312.0 Ω) than the CC-LFP electrode (120.1 Ω) and CC-LTO electrode (446.3 Ω), respectively, showing that the charge transfer kinetics of the electrode is improved by the acoustic-field-generated patterns. At the low-frequency region of the Nyquist plot, a tilted line was observed representing a Warburg impedance for semi-infinite linear diffusion. Warburg coefficient σ for the Warburg impedance can be obtained in the low-frequency region of the Nyquist plot by fitting the slope of the real part of impedance against $\omega^{-1/2}$ plot, as Fig. S15b and S15c illustrate. Using the Warburg coefficient σ, the diffusion coefficient of lithium ions (D_{Li^+}) can be calculated as detailed in the Electronic Supplementary Information. D_{Li^+} values calculated from the EIS data are listed in Table S3. D_{Li^+} in G-LFP and G-LTO electrode, for example, is 1.89×10^{-10} cm^2/s and 4.70×10^{-12} cm^2/s, respectively, and D_{Li^+} in L-LFP and L-LTO electrodes is 1.34×10^{-10} cm^2/s and 1.70×10^{-10} cm^2/s, respectively. Both acoustically processed electrodes have higher D_{Li^+} than the electrodes produced by CC method (CC-LFP: 3.67×10^{-11} cm^2/s, CC-LTO: 7.01×10^{-13} cm^2/s). The D_{Li^+} values calculated from EIS coincides with those calculated from CV and GITT measurements, which provides further evidence that improvement of lithium-ion diffusion is successfully achieved through the acoustically patterned structures in the electrodes. It is noted that the electrodes with grid patterns have slightly higher D_{Li^+} and lower R_{ct} compared with electrodes with line patterns, which explains the more superior electrochemical performance of the G-LFP and G-LTO electrodes compared with L-LFP and L-LTO.

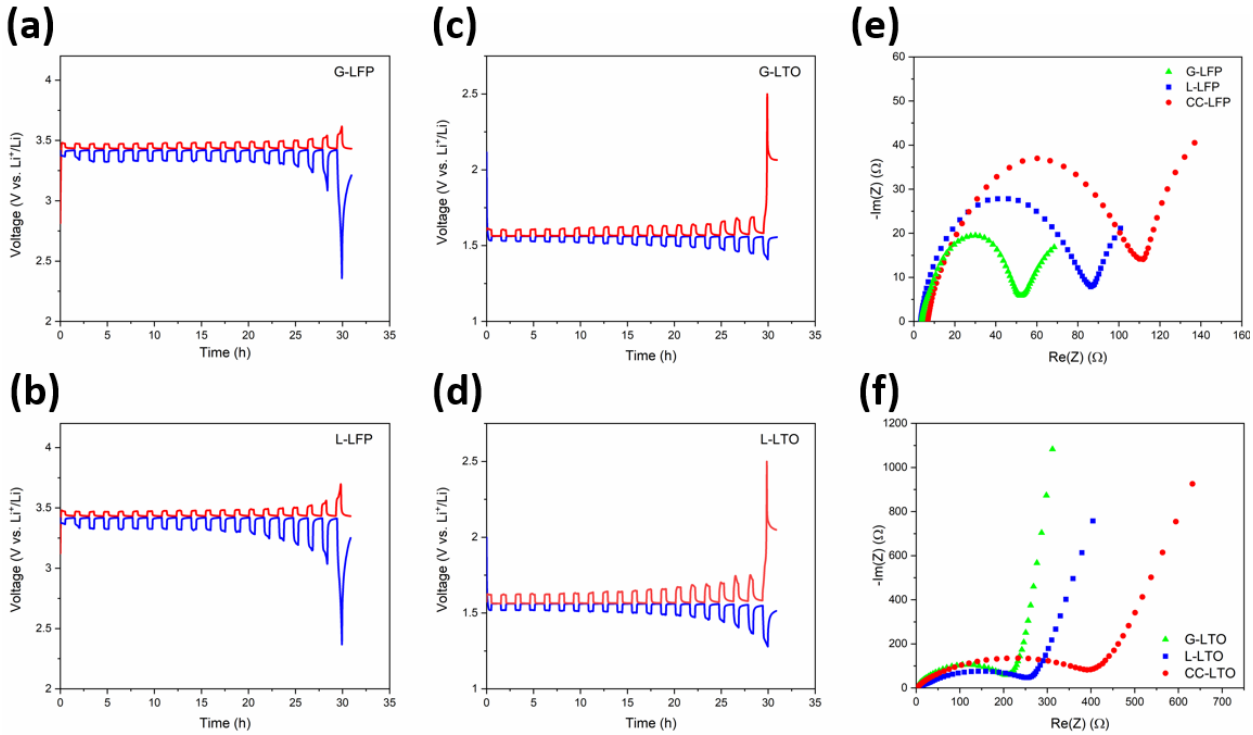

Fig. 6 GITT profiles of (a) G-LFP, (b) L-LFP, (c) G-LTO and (d) L-LTO; Nyquist plots of (e) LFP electrodes and (f) LTO electrodes.

Moreover, the rate capability of LFP and LTO electrodes with different structures were evaluated through half cells by pairing the as-prepared electrode with lithium chip as counter electrode. To compare the performance of electrodes produced by the acoustic-field-assisted and conventional casting method, the areal mass loading of all the electrodes was controlled as ~18 mg/cm^2. At low cycling rate of 0.1 C, the specific discharge capacity for all the acoustically patterned electrodes is slightly higher than the conventionally fabricated electrode. However, as the cycling rate increases, G-LFP electrode, for instance, exhibits higher discharge capacity of 158.5, 150.0, 131.8, 111.2 and 54.5 mAh/g at 0.5, 1, 2, 3 and 5 C, respectively, compared to CC-LFP, which has almost no capacity at 5 C. After high-rate charge and discharge cycles, G-LFP electrodes recover capacity of 164.8 mAh/g as current density returns to 0.1 C, which is approximately the same values as the ones in the initial five cycles. Such strengthened rate performance is also embodied by LTO electrodes produced by AP method. As the rate increased from 0.1 C to 2 C, all the LTO electrodes processed by acoustic field are capable of retaining more than 65% of capacity. Advantage with an even larger margin is demonstrated over the conventionally processed LTO electrode as the rate reached over 2 C. This series of comparison indicates the acoustic-field-assisted patterned structure in the electrodes aids to boost the rate capability of electrodes compared with conventional electrodes with the same areal mass loading. Additionally, full cells were assembled with LFP and LTO electrode with the same structures (line or grid) in each electrode. The cells comprised of grid-patterned, line-patterned and conventionally fabricated LFP and LTO are denoted as G-cell, L-cell and CC-cell. At C-rate ranging from 0.1 to 2 C, as shown in Fig. 7c, G-cell and L-cell both demonstrate advantageous rate performance over CC-cell. For the long-term cycling test (Fig. 7d), G-Cell and L-Cell retain 51.8 and 44.4 mAh/g after 200 cycles of charge and discharge at C/3 rate,

corresponding to capacity retention of 71.6% and 60.6%, respectively, while CC-cell only reaches 36.7 mAh/g, corresponding to capacity retention of only 53.4%. These results indicate improved cycling stability of electrodes with patterned structures. Considering all the results from the electrochemical characterizations, we can conclude that compared with conventionally fabricated electrodes, the enhanced rate capability and cycling stability of the acoustically processed electrodes are due to the improved lithium-ion diffusion and kinetics.

Considering that a calendering step was not applied before the electrochemical tests, the volumetric energy density of the acoustically processed electrodes could be slightly lower than that of the state-of-the-art calendered electrodes. From Fig. 7e, 7f and data shown in Table S4, however, the volumetric energy density of the acoustically processed electrodes is at a competitive level compared to the state-of-the-art electrodes used in LIBs and is higher than that of conventional electrodes at all C-rates, which indicates that the 3D-structured electrodes constructed by AP method do not sacrifice volumetric energy density to achieve capability at high rate[37]. To check if the ordered structures created by the acoustic patterning can survive the calendering step, we applied calendering to the electrodes fabricated by AP method, and the gap between the calendering rollers was set to 100-μm (the thickness of original samples: ~ 130-μm). The rolled samples were characterized by confocal microscopy and SEM, and the comparison between samples with and without calendering are shown in Fig. S16 and S17. From the confocal microscopy images, the acoustically generated "valleys" and "holes" are still visible after calendering. However, the width of the "valleys" and the "holes" both decrease after calendering. This is because the roll-press pushed some of the solid particles to fill part of the "valleys" and "holes". Such a change was validated by SEM images as the shrinkage of the widest part of the "valleys" and "holes" can be observed compared to the samples without calendering. In future, we will investigate how to jointly use acoustic particle patterning and calendering to tune the electrode properties for optimal electrochemical performances.

Finally, the charge/discharge profiles of electrodes at varied C-rates are illustrated in Fig. 8. LFP and LTO electrodes fabricated by the AP method deliver areal capacity up to 3.00 and 2.97 mAh/cm^2, respectively. The lower overpotentials between the charge and discharge plateau throughout the range of various C-rates for both types of active materials confirm the enhanced performances as a result of the ordered 3D structures in the electrodes. Furthermore, voltage profiles of the 2nd, 20th, 50th, 80th cycle of the full cells are demonstrated in Fig. S18. Like half-cell measurement, lower overpotential is also observed in the G-Cell and L-Cell as the cycling proceeds, which validates the enhanced cycling stability and electrochemical performance provided by the AP processed electrodes.

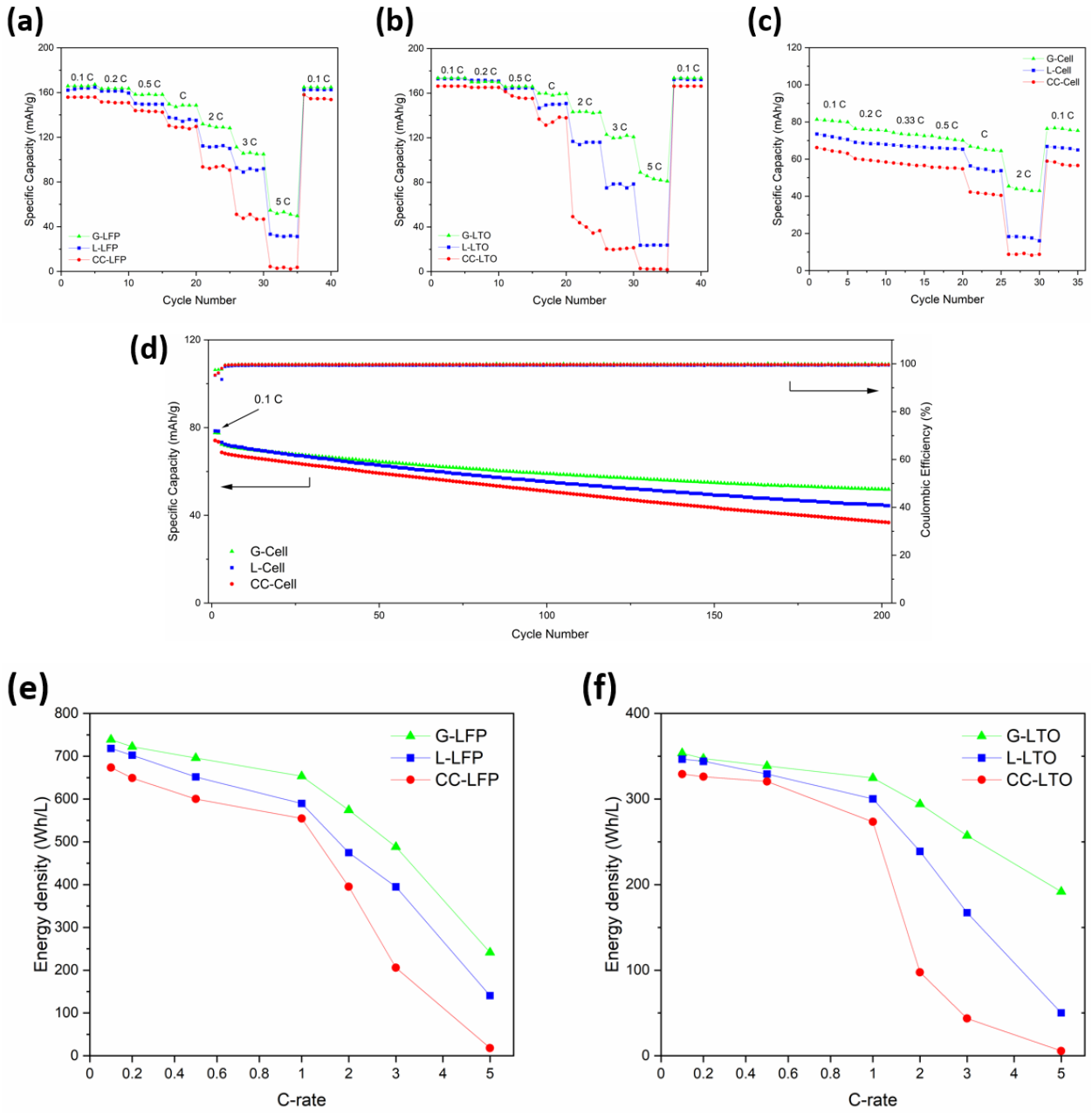

Fig. 7 (a) Rate performance of G-LFP, L-LFP and CC-LFP electrodes; (b) Rate performance of G-LTO, L-LTO and CC-LTO electrodes; (c) Rate performance of full-cells assembled by grid-patterned (G-Cell), line-patterned (L-Cell) and conventionally fabricated electrodes (CC-Cell); (d) Discharge capacity and coulombic efficiency of G-Cell, L-Cell and CC-Cell at rate of C/3. Volumetric energy density of (e) LFP and (f) LTO electrodes at various C-rates.

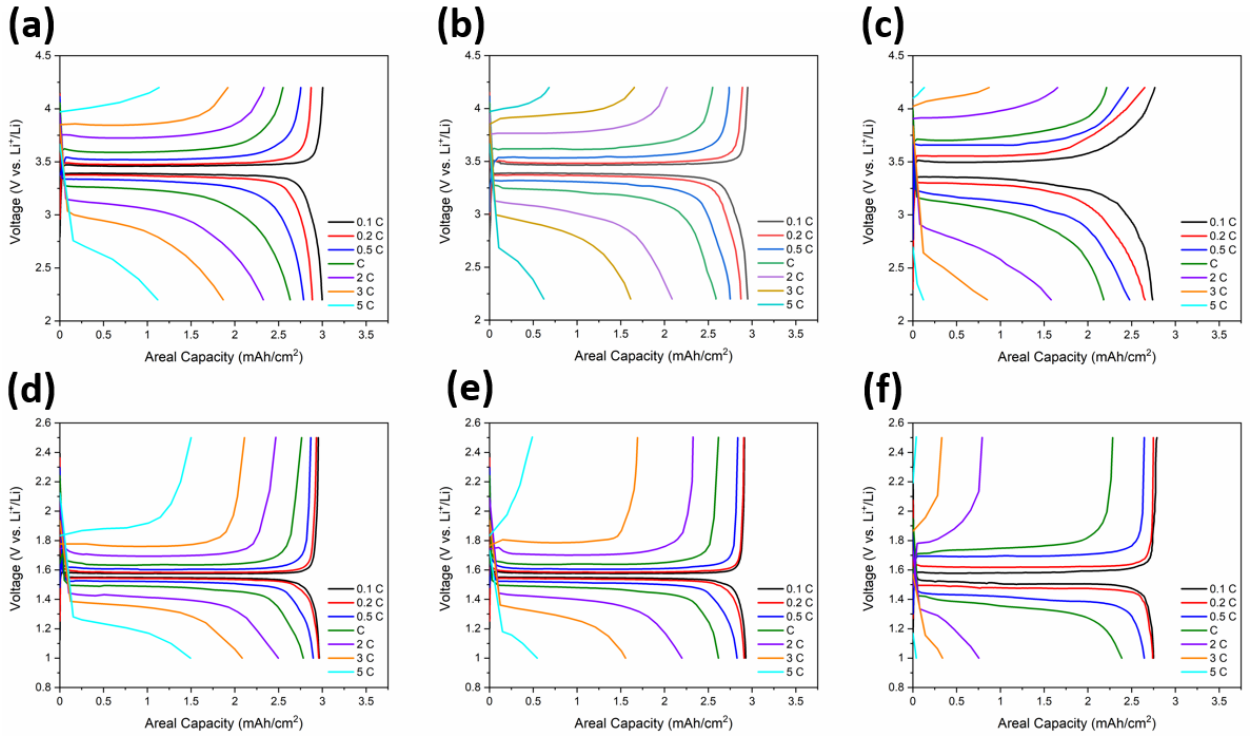

Fig. 8 Charge and discharge voltage profile of (a) G-LFP, (b) L-LFP, (c) CC-LFP, (d) G-LTO, (e) L-LTO and (f) CC-LTO.

4. Conclusion

In summary, using acoustic-field particle patterning, we successfully constructed ordered structures (aligned valleys and through-holes) in LFP and LTO based battery electrodes. This structural engineering approach enhances the lithium-ion diffusion and charge transfer kinetics in the electrodes. As a result, the acoustically patterned LFP and LTO electrodes demonstrate superior specific capacity at high rates of charge and discharge and advantageous long-term cycling stability compared to the ones fabricated by conventional casting method with similar areal mass loading. The acoustic-field-assisted manufacturing method does not require the use of expensive additives or complicated post-processing procedures, making the whole fabrication process more economical with less energy consumption. In addition, this method is applicable to pattern a wide range of solid components in the electrode slurry, which allows the opportunities to build 3D structured electrodes for both LIBs and beyond-lithium batteries to alleviate the limitation of mass transport in electrodes. With the combination of these advantages, this method represents a novel and effective strategy for enhancing the energy and power density of batteries, especially at relatively high rates. In future, the use of large-size PZTs will be explored to scale up the acoustic patterning areas and the combined use of acoustic patterning and calendaring will be investigated to further enhance the electrochemical performance of the acoustically processed electrodes.

Acknowledgements

This material is based upon work supported by the National Science Foundation under Grant No. 1752378. Any opinions, findings, and conclusions or recommendations expressed in this material are those of the authors and do not necessarily reflect the views of the National Science Foundation.

Conflict of Interest

The authors have no conflicts of interest.

References

1 N. Nitta, F. Wu, J. T. Lee and G. Yushin, *Mater. Today*, 2015, **18**, 252–264.
2 J. Li, J. Fleetwood, W. B. Hawley and W. Kays, *Chem. Rev.*, 2021, **122**, 903–956.
3 J. B. Goodenough and K.-S. Park, *J. Am. Chem. Soc.*, 2013, **135**, 1167–1176.
4 X. Zhang, Z. Ju, Y. Zhu, K. J. Takeuchi, E. S. Takeuchi, A. C. Marschilok and G. Yu, *Adv. Energy Mater.*, 2020, 2000808.
5 Y. Liu, Y. Zhu and Y. Cui, *Nat. Energy*, 2019, **4**, 540–550.
6 Y. Chen, B. Zhao, Y. Yang and A. Cao, *Adv. Energy Mater.*, 2022, 2201834.
7 Y. Kuang, C. Chen, D. Kirsch and L. Hu, *Adv. Energy Mater.*, 2019, **9**, 1901457.
8 I. V. Thorat, D. E. Stephenson, N. A. Zacharias, K. Zaghib, J. N. Harb and D. R. Wheeler, *J. Power Sources*, 2009, **188**, 592–600.
9 M. Ebner, D.-W. Chung, R. E. García and V. Wood, *Adv. Energy Mater.*, 2014, **4**, 1301278.
10 M. J. Lain and E. Kendrick, *J. Power Sources*, 2021, **493**, 229690.
11 H. Zheng, J. Li, X. Song, G. Liu and V. S. Battaglia, *Electrochim. Acta*, 2012, **71**, 258–265.
12 Z. Du, D. L. Wood, C. Daniel, S. Kalnaus and J. Li, *J. Appl. Electrochem.*, 2017, **47**, 405–415.
13 K.-H. Chen, M. J. Namkoong, V. Goel, C. Yang, S. Kazemiabnavi, S. M. Mortuza, E. Kazyak, J. Mazumder, K. Thornton, J. Sakamoto and N. P. Dasgupta, *J. Power Sources*, 2020, **471**, 228475.
14 L. Li, R. M. Erb, J. Wang, J. Wang and Y. M. Chiang, *Adv. Energy Mater.*, 2019, **9**, 1802472.
15 J. S. Sander, R. M. Erb, L. Li, A. Gurijala and Y. M. Chiang, *Nat. Energy*, 2016, **1**, 16099.
16 J. Billaud, F. Bouville, T. Magrini, C. Villevieille and A. R. Studart, *Nat. Energy*, 2016, **1**, 16097.
17 J. Ma, Y. Qiao, M. Huang, H. Shang, H. Zhou, T. Li, W. Liu, M. Qu, H. Zhang and G. Peng, *Appl. Surf. Sci.*, 2021, **542**, 148664.
18 J. Wu, Z. Ju, X. Zhang, X. Xu, K. J. Takeuchi, A. C. Marschilok, E. S. Takeuchi and G. Yu, *ACS Nano*, 2022, **16**, 4805–4812.
19 D. Dang, Y. Wang, S. Gao and Y.-T. Cheng, *Carbon*, 2020, **159**, 133–139.
20 Y. Hwa, E. Yi, H. Shen, Y. Sung, J. Kou, K. Chen, D. Y. Parkinson, M. M. Doeff and E. J. Cairns, *Nano Lett.*, 2019, **19**, 4731–4737.
21 G. Du, Y. Zhou, X. Tian, G. Wu, Y. Xi and S. Zhao, *Appl. Surf. Sci.*, 2018, **453**, 493–501.
22 Y. Guo, Y. Jiang, Q. Zhang, D. Wan and C. Huang, *J. Power Sources*, 2021, **506**, 230052.
23 X. Zhang, Z. Hui, S. King, L. Wang, Z. Ju, J. Wu, K. J. Takeuchi, A. C. Marschilok, A. C. West, E. S. Takeuchi and G. Yu, *Nano Lett.*, 2021, **21**, 5896–5904.
24 C. Huang, M. Dontigny, K. Zaghib and P. S. Grant, *J. Mater. Chem. A*, 2019, **7**, 21421–21431.
25 B. Delattre, R. Amin, J. Sander, J. De Coninck, A. P. Tomsia and Y.-M. Chiang, *J. Electrochem. Soc.*, 2018, **165**, A388–A395.

26 X. Zhang, Z. Ju, L. M. Housel, L. Wang, Y. Zhu, G. Singh, N. Sadique, K. J. Takeuchi, E. S. Takeuchi, A. C. Marschilok and G. Yu, *Nano Lett.*, 2019, **19**, 8255–8261.
27 S. Yang, C. Zhou, Q. Wang, B. Chen, Y. Zhao, B. Guo, Z. Zhang, X. Gao, R. Chowdhury, H. Wang, C. Lai, N. P. Brandon, B. Wu and X. Liu, *Energy Environ. Mater.*, 2022, **5**, 1332–1339.
28 X. Ding, P. Li, S.-C. S. Lin, Z. S. Stratton, N. Nama, F. Guo, D. Slotcavage, X. Mao, J. Shi, F. Costanzo and T. J. Huang, *Lab Chip*, 2013, **13**, 3626–3649.
29 H. Bruus, *Lab Chip*, 2012, **12**, 1014–1021.
30 K. Melde, E. Choi, Z. Wu, S. Palagi, T. Qiu and P. Fischer, *Adv. Mater.*, 2017, **30**, 1704507.
31 Z. Ma, A. W. Holle, K. Melde, T. Qiu, K. Poeppel, V. M. Kadiri and P. Fischer, *Adv. Mater.*, 2020, **32**, 1904181.
32 D. E. Yunus, S. Sohrabi, R. He, W. Shi and Y. Liu, *J. Micromechanics Microengineering*, 2017, **27**, 045016.
33 L. Lu, X. Tang, S. Hu and Y. Pan, *3D Print. Addit. Manuf.*, 2018, **5**, 151–159.
34 P. Zhang, H. Bachman, A. Ozcelik and T. J. Huang, *Annu. Rev. Anal. Chem.*, 2020, **13**, 17–43.
35 P. L. M. J. van Neer, A. Rasidovic and A. W. F. Volker, in *2013 IEEE International Ultrasonics Symposium (IUS)*, IEEE, 2013, pp. 1915–1918.
36 M. Shahriar, Y. H. Lui, B. Zhang, K. Lichade, Y. Pan and S. Hu, *ACS Appl. Mater. & Interfaces*, 2022, **14**, 44782–44791.
37 J. Chang, Q. Huang, Y. Gao and Z. Zheng, *Adv. Mater.*, 2021, **33**, 2004419.